





## Article

# Joint Analysis of the Iron Emission in the Optical and Near-Infrared Spectrum of I Zw 1

Denimara Dias dos Santos<sup>1,2,\*</sup> , Swayamtrupta Panda<sup>3,\*</sup> , Alberto Rodríguez-Ardila<sup>1,3</sup>   
and Murilo Marinello<sup>3</sup> 

<sup>1</sup> Divisão de Astrofísica, Instituto Nacional de Pesquisas Espaciais (INPE), Avenida dos Astronautas 1758, São José dos Campos 12227-010, SP, Brazil; aardila@lna.br

<sup>2</sup> Istituto Nazionale di Astrofisica (INAF), Osservatorio Astronomico di Padova, 35122 Padova, Italy

<sup>3</sup> Laboratório Nacional de Astrofísica (LNA), Rua dos Estados Unidos 154, Bairro das Nações, Itajubá 37504-364, MG, Brazil; murilo.marinello@gmail.com

\* Correspondence: denimara.santos@inpe.br (D.D.d.S.); spanda@lna.br (S.P.)

**Abstract:** Constraining the physical conditions of the ionized media in the vicinity of an active supermassive black hole (SMBH) is crucial to understanding how these complex systems operate. Metal emission lines such as iron (Fe) are useful probes to trace the gaseous media's abundance, activity, and evolution in these accreting systems. Among these, the FeII emission has been the focus of many prior studies to investigate the energetics, kinematics, and composition of the broad-emission line region (BELR) from where these emission lines are produced. In this paper, we present the first simultaneous FeII modeling in the optical and near-infrared (NIR) regions. We use CLOUDY photoionization code to simulate both spectral regions in the wavelength interval 4000–12,000 Å. We compare our model predictions with the observed line flux ratios for I Zw (Zwicky) 1—a prototypical strong FeII-emitting active galactic nuclei (AGNs). This allows setting constraints on the BLR cloud density and metal content that is optimal for the production of the FeII emission, which can be extended to I Zw 1-like sources by examining a broad parameter space. We demonstrate the salient and distinct features of the FeII pseudo-continuum in the optical and NIR, giving special attention to the effect of micro-turbulence on the intensity of the FeII emission.

**Keywords:** active galaxies; quasars; emission lines; supermassive black holes; thermal radiation mechanisms; radiative transfer; infrared spectroscopy; emission line observational methods; spectral numerical simulations; spectroscopic techniques in astrophysics



**Citation:** Dias dos Santos, D.; Panda, S.; Rodríguez-Ardila, A.; Marinello, M. Joint Analysis of the Iron Emission in the Optical and Near-Infrared Spectrum of I Zw 1. *Physics* **2024**, *6*, 177–193. <https://doi.org/10.3390/physics6010013>

Received: 15 November 2023

Revised: 30 December 2023

Accepted: 5 January 2024

Published: 5 February 2024



**Copyright:** © 2024 by the authors. Licensee MDPI, Basel, Switzerland. This article is an open access article distributed under the terms and conditions of the Creative Commons Attribution (CC BY) license (<https://creativecommons.org/licenses/by/4.0/>).

## 1. Introduction

Active galactic nuclei (AGNs) are harbored within the central cores of galaxies and host active supermassive black holes (SMBHs) at their very centers. The radiation originates from the heating of material that is drawn toward the SMBH and subsequently triggers ionization within the gas and metal-rich environment surrounding these systems [1,2]. The appearance of AGNs can vary based on the observer's perspective due to their intricate geometry [3,4]. This phenomenon also becomes evident in their observed spectra.

AGNs are further classified in terms of the types of emission line profiles they demonstrate in their observed spectrum. Sources displaying a combination of broad (permitted and semi-permitted) as well as narrow forbidden emission line profiles are categorized as Type-I sources, while those lacking broad emission lines are classified as Type-II [1,5–7]. This study exclusively concentrates on Type-I sources and their emissions. The origin of the broad emission lines can be traced back to a region located around 0.01–0.1 parsecs away from the central ionizing source. This measurement is derived through the widely recognized technique of reverberation mapping, which has been applied to a substantial sample of over 200 AGNs to date [8–14]. This region, known as the broad line region

(BLR), contributes significantly to the emissions observed in a typical Type-I AGN spectrum [10,11,15–36]. Notably, among the salient BLR emission features is the FeII emission, encompassing a wavelength range from ultraviolet (UV) to near-infrared (NIR) [37–39].

The emission from FeII is remarkable in the Type-I AGN spectra, primarily due to the aggregation of an extensive array of transitions—above 344,000 in number. The accumulation of the lines mimics a continuum and is hence known as a pseudo-continuum in an AGN spectrum [38,40–42]. The large number of emissions stemming from the FeII ion play a pivotal role in characterizing the energy distribution within the BLR—approximately 25% of the total emission originating in the BLR is attributed to the FeII lines [37]. Succeeding investigations have confirmed the utility of FeII emission as a surrogate for quantifying metal abundances in the BLR of AGNs across a broad range of redshifts, contributing to insights into the evolutionary trends of metallic elements within these galaxies [4,43–46].

Another crucial outcome from studies centered on FeII pertains to the development of emission templates specific to FeII. From a purely observational standpoint, the pioneering paper [47] by Todd Boroson and Richard Green marked the inception of extracting FeII emissions from a quintessential AGN FeII emitter, I Zw (Zwicky) 1, which itself has a long and rich history [40,48–54]. The FeII template was meticulously constructed by isolating and excluding all emission lines except in the FeII. This template-driven approach continues to be employed across various studies, serving as the foundation for quantifying the optical intensity of FeII. In Ref. [47], the authors also established a robust association between the strength of FeII and various attributes of both the BLR and the narrow line region (NLR). Employing principal component analysis (PCA)—a dimensionality reduction technique—multiple correlations between observed spectroscopic parameters were identified. Eigenvector 1 (EV1) was the paramount correlation space among those multiple correlations. The EV1 from the study in Ref. [47] shows a strong correlation between the optical FeII emission within the spectral range of 4434–4684 Å (centered at the wavelength 4570 Å), the peak intensity of [OIII]λ5007 oxygen emission line and the full width at half maximum (FWHM) of the broad component of the Balmer Hβ hydrogen emission profile. This led to the well-defined FWHM(Hβ) versus  $R_{\text{FeII}}$  connection ( $R_{\text{FeII}}$  generally denotes the ratio of the integrated FeII emission within 4434–4684 Å to the broad Hβ emission), that is, the well-known optical plane of the quasar main sequence [4,24,26,55–58]. Within this framework, FeII emission not only plays a crucial role in discerning the underlying factors driving EV1 [4] but also serves as a link between line strength and the emitting gas physics for a diverse population of Type-1 AGNs along the EV1 plane.

Regarding FeII templates, Marianne Vestergaard and Belinda Wilkes progressed [59] in the UV domain by extending the template methodology into the ultraviolet spectrum using a high-quality HST/FOS (Hubble Space Telescope/Faint Object Spectrograph) spectrum for I Zw 1. Subsequent efforts have since created several templates, effectively characterizing UV-optical FeII emission across large samples of AGNs [60–64]. In Ref. [64], an innovative optical FeII template was derived through a semi-empirical approach, combining the observed FeII emission with theoretical predictions based on allowed transitions between energy levels for the ion. By meticulously measuring individual FeII multiplet groups, the study [64] achieved a better overall agreement and was successful in obtaining an improved estimate for the  $R_{\text{FeII}}$ . Reproducing FeII emission in sources similar to I Zw 1 has been challenging, as empirical templates struggle to replicate specific features in observed spectra. In a recent development, Ref. [54] introduced a new template based on the Mrk (Markarian) 493 AGN spectrum to improve the modeling of FeII emission in I Zw 1-like sources.

Significant strides in predicting near-infrared (NIR) FeII spectra were accomplished in Refs. [41,65] through the utilization of the Lyα (Lyman-alpha) fluorescence excitation mechanism to elucidate FeII emissions within the wavelength range of 8500–9500 Å. This Lyα process exclusively governs the stimulation of energy levels reaching up to 13.6 eV, giving rise to the emission lines observed within this spectral segment. Such assertion was corroborated by observations conducted in Ref. [66]. A semi-empirical template for NIR FeII

emissions was later developed in Ref. [67] by combining an observed spectrum of I Zw 1 with theoretical models from prior studies [41,42,65]. More recently, this semi-empirical template was successfully applied in the NIR Fe II modeling in several AGN spectra [39,68].

It is worth noting here that the NIR spectrum exhibits FeII emission lines that are either isolated or semi-isolated, in contrast to the UV-optical region (see Figure 1). This feature provides a distinct advantage by enabling a more precise and reliable determination of the FeII emission line properties. The FeII lines around the 1-micron region at the wavelengths  $\lambda 9997 \text{ \AA}$ ,  $\lambda 10502 \text{ \AA}$ ,  $\lambda 10863 \text{ \AA}$ , and  $\lambda 11127 \text{ \AA}$  are the most intense among the FeII lines [66,69,70].

Recent research [68] has highlighted the intrinsic correlation between FeII emission in the optical and near-infrared spectral regions. Due to the intricacies of FeII ion's behavior and the challenges associated with modeling its emission, researchers have been prompted to explore alternative approaches for investigating the FeII emitting gas [71,72]. Observational and photoionization modeling works have been indicating that less complex ions, such as CaII triplet, CaT ( $\lambda 8498 \text{ \AA}$ ,  $\lambda 8542 \text{ \AA}$ , and  $\lambda 8662 \text{ \AA}$ ), and OI lines at  $\lambda 8446$  and  $\lambda 11287$ , can serve as proxies for studying the spatial distribution of FeII emitting gas [66,68,71–73].

The FeII emission is dependent on the BLR temperature and gas density, and also on other parameters such as composition and Brownian motion within the BLR cloud—high temperature (about 5000 K–10,000 K), relatively high density ( $\log n_{\text{H}} = 10\text{--}12 \text{ cm}^{-3}$ ), super-solar abundances and micro-turbulence of the order of  $\sim 100 \text{ km s}^{-1}$  have been shown to positively impact the production of the FeII emission, especially in the UV and optical spectra regions [4,44,74,75]. In a recent study [76], we assessed the NIR FeII emission in I Zw 1 under a low column density regime ( $10^{22} \text{ cm}^{-2}$ ). In this current study, we perform a comprehensive analysis of the influence of micro-turbulence on NIR emissions over a broad range of cloud densities and metal content in conjunction with the optical region in a high column density regime ( $10^{24} \text{ cm}^{-2}$ ).

We model the FeII emission to understand the line formation and the nature of the physical conditions in AGN with strong FeII emissions, exploring how changing metal content and micro-turbulence effectively increase the FeII optical and NIR emissions simultaneously. For this purpose, we investigate three cases of micro-turbulence velocities within the ionized media, namely of 0, 10, and  $100 \text{ km s}^{-1}$  (based on the previous study [73], which focused only on recovering the optical FeII emission). The inclusion of the micro-turbulence parameter has been shown to augment the FeII emission line intensity in the optical and UV regions due to the increase in the overall random, Brownian motion of the ions within the cloud [46,75,77]. Here, we perform the first study that tests the effect of micro-turbulence and metal content on the production of NIR FeII emission, along with the optical FeII emission.

The paper is organized as follows. Section 2 presents the observational spectroscopic data in the optical and NIR regimes for I Zw 1. Section 3 describes the extraction of the FeII emission in the optical and NIR regimes and the estimation of the corresponding FeII strengths from the observed spectra. In Section 4, we demonstrate the modeling setup using the photoionization code CLOUDY [78]. Results are highlighted in Section 5, followed by a brief discussion in Section 6. We summarize our findings from this study in Section 7.

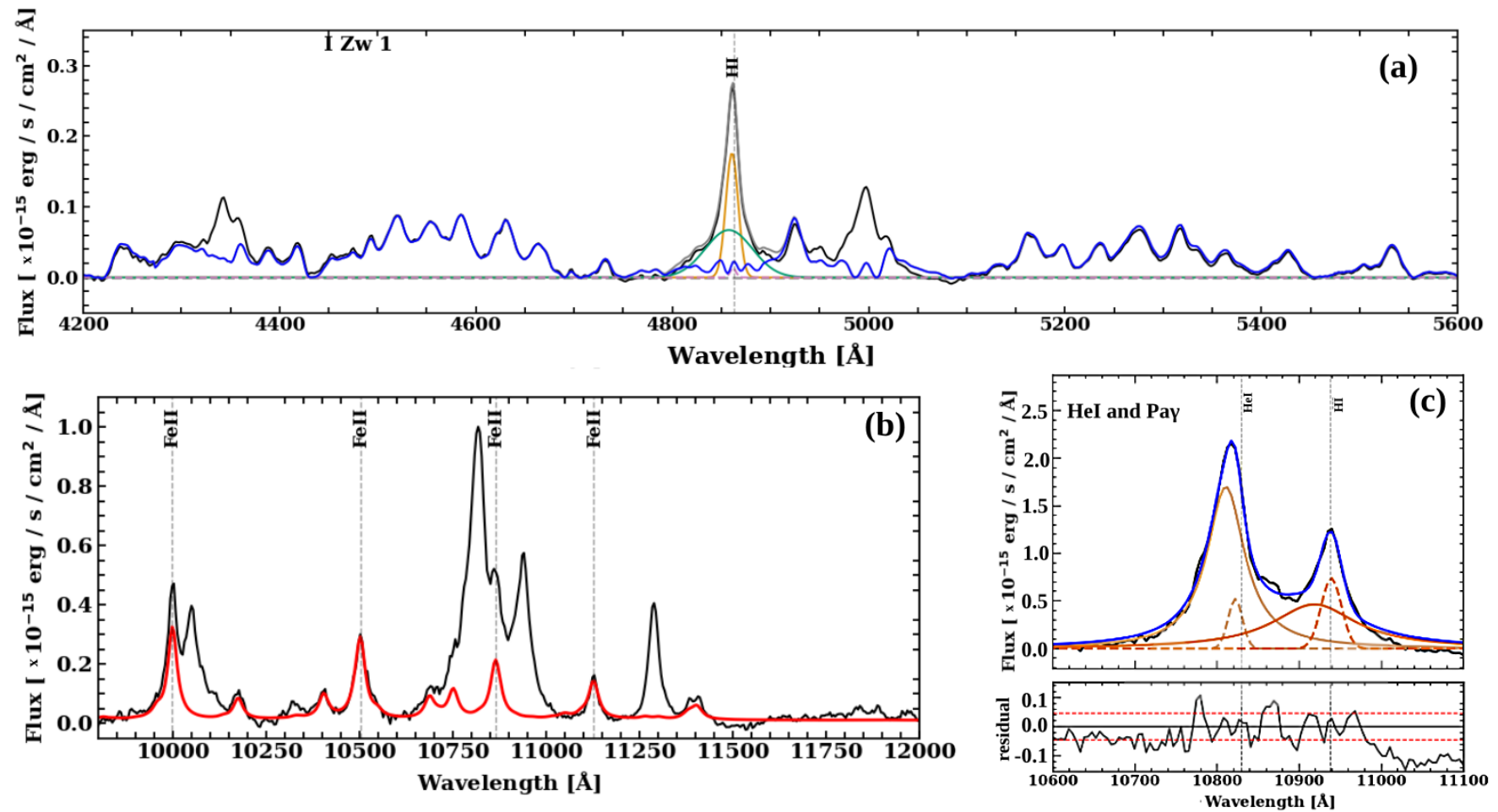


**Figure 1.** Spectra of galaxy, I Zw 1. (a) The observed optical spectrum (in black) along with those with H $\beta$  emission line fits the outflow (green), BLR (yellow), and faint narrow (dashed orange) components. The blue curve represents the optical FeII template. (b) The measured near-infrared spectrum (in black) along with the fit to the semi-empirical [67] template (red), highlighting four main NIR FeII lines used to estimate the 1-micron intensity. (c) The Pa $\gamma$ -HeI line blended with HeI for the observed spectrum (in black) and the fits to the BLR (solid orange) and NLR components. See text for details.

## 2. I Zw 1 a Prototypical FeII Emitter

The I Zw 1 is a nearby (with the redshift  $z = 0.061$ ) narrow-line Seyfert 1 galaxy (NLS1), considered a prototypical FeII emitter and widely studied in the literature [37,59,69,79,80]. NLS1s, a subclass of classical Type-I AGNs, display a narrower-to-broader range of  $H\beta$  line widths compared to classical Seyfert-I galaxies, which typically feature  $\text{FWHM}(H\beta) < 2000 \text{ km s}^{-1}$  and a flux ratio,  $[\text{OIII}]\lambda 5007/H\beta < 3$  [81].

The I Zw 1 spectrum has a rich historical record of UV, optical, and NIR studies [47,59,64,67]. Recent reverberation mapping estimated the BLR's distance of the line-emitting BLR from the central ionizing source,  $R_{\text{BLR}} = 37.2$  light-days [80], a crucial parameter that allows minimizing the degeneracies in our numerical simulations.

To perform the optical and NIR analysis, we use the reduced and available spectra of the I Zw 1 from previous studies [66–68,70]. The NIR spectrum was observed using the 3.2-m IRTF telescope (NASA, U.S. National Aeronautics and Space Administration, Infrared Telescope Facility, Washington, DC, USA) at Mauna Kea, Hawaii-USA in 2000. It employed the SpeX spectrograph in cross dispersion mode (SXD) covering the wavelength interval 0.8–2.4 microns, and photometric near-infrared bands zJHK, with a spectral resolution,  $R = 2000$  corresponding to the  $0.8'' \times 15''$  slit. The papers [66,70] provide detailed information on the reduced spectrum and the related observational. The optical counterpart region was obtained from Ref. [66]. The optical spectrum was obtained at the CASLEO Observatory (Complejo Astronómico el Leoncito, San Juan, Argentina), employing the REOSC spectrograph (Saint-Pierre-du-Perray, France) in long slit mode covering the range 3500–6800 Å with a resolution of  $0.10 \text{ Å pixel}^{-1}$ .

## 3. Optical and NIR FeII Templates

The FeII pseudo-continuum comprises a multitude of permitted FeII lines spanning from the UV to the NIR spectral regions, necessitating the use of templates for accurate modeling. In the optical domain, we used the empirical FeII template by Boroson and Green [47] derived from the spectrum of I Zw 1, the archetypal NLS1 galaxy. In the NIR range, we employed the semi-empirical template from Ref. [67]. These models encompass approximately 1915 lines, within the wavelength range of 8000–11,600 Å. The FeII spectrum was synthesized using the template, where we first widened it based on the width of the 10,502 Å line and then scaled the template to match the observed spectrum. We used the 10,502 Å line as it is the most isolated FeII line in this region, thus allowing for accurate measurement of the overall FeII intensity. The best-fit template was determined by minimizing the chi-square value at 10,502 Å. Figure 1 illustrates the spectral fitting and component decomposition for the optical and NIR region for I Zw 1. The estimation of flux uncertainty is based on the standard deviation of the best-fitted model, considering the spectrum within  $3\sigma$  (standard deviations) of the line of interest. For the ratios, we employed error propagation to estimate their uncertainties (see Table 1). In NLS1s, BLR emission line profiles are best represented using Lorentzian, while those of Type-I AGN with broader lines follow Gaussian shapes [82]. We fit the emission lines using the LMFIT library from the Python programming package, employing Lorentzian profiles to represent the BLR components, where the  $\chi^2$ -fit minimizes the residual left after subtraction of the fitted profile. For lines emitted by the NLR, we employ only Gaussian components. This procedure enabled us to measure the integrated flux, FWHM, and centroid position of the lines of interest.

**Table 1.** Characteristics measured from the near-infrared and optical spectra of I Zw 1, where the fluxes are given in  $10^{-14} \text{ erg s}^{-1} \text{ cm}^{-2} \text{ Å}^{-1}$  units. See text for details.

$\text{FeII}\lambda 10502$	$\text{FeII}\lambda 9998$	$\text{FeII}\lambda 10863$	$\text{FeII}\lambda 11127$	$\text{Pa}\gamma$	$R_{1\mu\text{m}}$	$H\beta$	$\text{FeII}\lambda 4570$	$R_{4570}$
$2.70 \pm 1.38$	$4.13 \pm 1.06$	$0.150 \pm 0.17$	$2.32 \pm 1.29$	$5.96 \pm 0.83$	$0.46 \pm 0.47$ to $1.48 \pm 0.15$	$10.30 \pm 1.84$	$16.70 \pm 2.80$	$1.62 \pm 0.06$



From the spectra and template fits, we obtained the optical FeII and NIR intensities and their ratios to the nearest hydrogen line, where for the optical FeII we obtained  $R_{4570} = 1.62 \pm 0.06$ . The  $R_{4570}$  is defined as the ratio of the flux of optical FeII multiplets 37, 38, within the wavelength range 4434–4684 Å to the flux of the H $\beta$  broad component [7,47]. Our finding is similar to that from previous studies:  $\sim 1.47$  [7].

For the 1-micron ratio,  $R_{1\mu\text{m}}$ , we observed a discrepancy between our finding and the result  $R_{1\mu\text{m}} = 1.81 \pm 0.08$ , reported in Ref. [68]. The  $R_{1\mu\text{m}}$  is calculated as the ratio of the combined fluxes from the four noticeable NIR isolated FeII lines at the wavelengths  $\lambda 9997$ ,  $\lambda 10502$ ,  $\lambda 10863$ , and  $\lambda 11127$  to the flux of Paschen hydrogen Pa $\beta$  broad component [66]. To stress is that the value of 1.81 is taken from the study [68] and not obtained in current investigation. The value, obtained in our analysis, is much smaller, see Table 1. The difference to be attributed to differing methodologies employed in the two studies. Specifically, Ref. [68] estimated measurements corresponding to Pa $\alpha$  emission lines and utilized the theoretical lines' ratio from [67] to re-scale to Pa $\beta$  intensity. In contrast, our approach involves the estimation of the flux of the broad component of Pa $\gamma$ . We opted for the utilization of Pa $\gamma$  rather than Pa $\beta$ , as the latter is situated within a telluric spectral region; see, e.g., [39].

We investigated how the ratio between Pa $\gamma$  and Pa $\beta$  evolves under varying gas physical conditions from our CLOUDY simulations (see Figure A1) instead of using the theoretical value for Pa $\beta$ /Pa $\gamma$  (i.e., 0.8531). In Figure A1, we highlight the dependence of the ratio on the cloud density as a function of the range of metal content that is assumed in this work using CLOUDY photoionization code. The value of the Pa $\beta$ /Pa $\gamma$  ratio varies between 1.05 and 3.38. We assumed a fixed column density (of  $10^{24} \text{ cm}^{-2}$ ) with no micro-turbulence for this analysis. We then derived the  $R_{1\mu\text{m}}$  estimates based on the calculated minimum and maximum value of the ratios obtained from the simulations, which we detail in Section 4. We re-scaled the Pa $\gamma$  observed flux to obtain the flux for Pa $\beta$  (for the minimum and maximum values of their ratio) and estimated the minimum and maximum values for the intensity of FeII 1-micron lines. Consequently, we obtained a range of values for  $R_{1\mu\text{m}} = 0.46 \pm 0.47$  and  $1.48 \pm 0.15$ , respectively.

#### 4. Photoionization Modeling

The range of the physical conditions used in this study was based on previous approaches [72,73,76]. We employed the default model for the FeII ion in CLOUDY, i.e., the one defined in Ref. [38], which includes 371 levels, ranging in energy up to 11.6 eV, and 68,635 transitions to maintain consistency with previous studies in low column density regime [76].

We performed numerical simulations using CLOUDY v17.03 [78]. To constrain the number of free parameters to three, we adopted the following fixed values: the luminosity at 5100 Å,  $L_{5100} = 3.19 \times 10^{44} \text{ erg s}^{-1}$  from Ref. [83], the BLR radius determined via reverberation mapping,  $R_{\text{BLR}} = 37.2$  light-days, based on Ref. [80], and a cloud column density,  $N_{\text{H}} = 10^{24} \text{ cm}^{-2}$  as concluded from earlier studies involving the recovery of the optical FeII emission in this source [72,84]. Furthermore, we adopted the spectral energy distribution for I Zw 1 from Ref. [72] as the radiation field in our simulations. Thus, the remaining free parameters are: (i) the cloud mean hydrogen density,  $n_{\text{H}}$ , which ranges between  $10^9$  and  $10^{14} \text{ cm}^{-3}$  and (ii) the metal content ( $Z$ ) in the cloud in the range of  $0.1 \leq Z \leq 10$  (in solar units), estimated using the GASS10 module [85]. Moreover, we incorporated two scenarios for internal random motions within the BLR clouds, specifically micro-turbulence (with the velocity,  $V_{\text{turb}}$ ) of 10 and 100  $\text{km s}^{-1}$ . The micro-turbulence in the BLR is caused by random motions of photons within the ionized gas, which is likely triggered by magnetic fields in the confined clouds [86,87] and acts as a secondary contributor to the overall line width, as has been shown in previous studies (e.g., [88]). We assumed the values for the micro-turbulent velocity based on previous studies, which were successful in modeling the FeII emission in the UV region for I Zw 1 for about 10–30  $\text{km s}^{-1}$  [74]. In addition, in Refs. [75,84], it is found that a micro-turbulence velocity between 10 and 100  $\text{km s}^{-1}$  can reproduce the FeII emission in the optical region. Additionally, as here we compare

the effect of using micro-turbulence in the gas, we performed simulations in the absence of micro-turbulence in the gas ( $V_{\text{turb}} = 0 \text{ km s}^{-1}$ ). This results in a total of 609 model combinations:  $V_{\text{turb}} \times n_{\text{H}} \times Z = 3 \times 29 \times 7$ .

## 5. Results

We derived the optical FeII and the NIR FeII ratios from the CLOUDY simulations, denoted as  $R_{4570}$  and  $R_{1\mu\text{m}}$ , respectively. Refs. [66,68] demonstrate that the optical and NIR intensities are correlated, indicating that both emissions should have origin and excitation mechanisms in common.

The micro-turbulence effect has been extensively studied in the optical FeII emission, [73,74], while was not performed in the NIR. In this paper, we study the micro-turbulence effect applied to the NIR FeII region for the first time. The results are shown in Figure 2 for the column density scenario of  $10^{24} \text{ cm}^{-2}$  for the optical (Figure 2a–c) and NIR (Figure 2d–f) spectral regions. The diagnostic diagrams in Figure 2 show the outcomes for  $V_{\text{turb}}$  values of 0, 10, and 100  $\text{km s}^{-1}$ , for  $R_{4570}$  and  $R_{1\mu\text{m}}$  intensities as a function of the local cloud density. Figure 2 demonstrates how the intensities vary with different metal content levels in the BLR clouds depicted by the color gradient. We further highlight the observed ratios,  $R_{4570}$  and  $R_{1\mu\text{m}}$ , and their associated uncertainties, obtained by fitting the observed spectra within the gray and titan white shaded regions, respectively.

### 5.1. No Micro-Turbulence

Our result without micro-turbulence (i.e., at  $V_{\text{turb}} = 0 \text{ km s}^{-1}$ ) is shown in Figure 2a,d, where the simulated results from CLOUDY are compared with the observed values for optical and NIR,  $R_{4570} = 1.62 \pm 0.06$  and  $R_{1\mu\text{m}} = 0.46\text{--}1.48$ , represented by the gray and titan white bands, respectively (the symmetric errors for 1-micron values are 0.15 and 0.47, respectively, also shown in Table 1). Here, the widths of the gray bands account for the uncertainties associated with the ratios. The results show that  $R_{4570}$  can be reproduced with a metal content above  $3 Z_{\odot}$  and with a local hydrogen density between  $10^{10.75}$  and  $10^{12.50} \text{ cm}^{-3}$ . Moreover, from the NIR results, to reproduce  $R_{1\mu\text{m}}$ , one needs local hydrogen densities to range from  $10^{9.00}$  to  $10^{11.50} \text{ cm}^{-3}$ , and a metal content above  $3 Z_{\odot}$ . These results demonstrate a suitable physical parameters range to be able to reproduce the FeII strengths for I Zw 1 in the optical and NIR regimes within the setup considered here.

### 5.2. Applying Micro-Turbulence

Previous studies [72,74] demonstrated that the value obtained for  $R_{4570}$  in high metal content simulations can be achieved by increasing the micro-turbulent velocity. To investigate how changing metallicity and micro-turbulence can increase both optical and NIR emissions simultaneously, we included two cases of micro-turbulent velocity at 10 and 100  $\text{km s}^{-1}$  and compare this cases with the default case (i.e., with no micro-turbulence).

One would expect that the micro-turbulence in the gas would increase the Brownian motion within the cloud and allow for the FeII ions to receive preferentially more ionizing photons, consequently leading to an increase in the intensity of the FeII lines.

The results using micro-turbulence of 10 and 100  $\text{km s}^{-1}$  are shown in Figure 2b,e and Figure 2c,f, respectively. Our results for the optical region reveal that the FeII at 4570 Å strength increases with the increase in micro-turbulence, as expected from earlier investigations [72,73].

On the other hand, the results in the NIR show a different behavior compared to the ones in the optical, as presented in Figure 2. Considering a single case with  $n_{\text{H}} = 10^{12} \text{ cm}^{-3}$ , solar metallicity, and  $V_{\text{turb}} = 10 \text{ km s}^{-1}$  (see Figure 2e),  $R_{1\mu\text{m}}$  is approximately 0.2, whereas at 100  $\text{km s}^{-1}$ , it dropped to about 0.05 (see Figure 2f). In contrast, the case with no micro-turbulence produces a  $R_{1\mu\text{m}}$  value of about 0.1 (see Figure 2d). Notably, the absence of micro-turbulence results in lower  $R_{1\mu\text{m}}$  values compared to the scenario with  $V_{\text{turb}} = 10 \text{ km s}^{-1}$ , as expected, based on the results obtained in the optical regime.

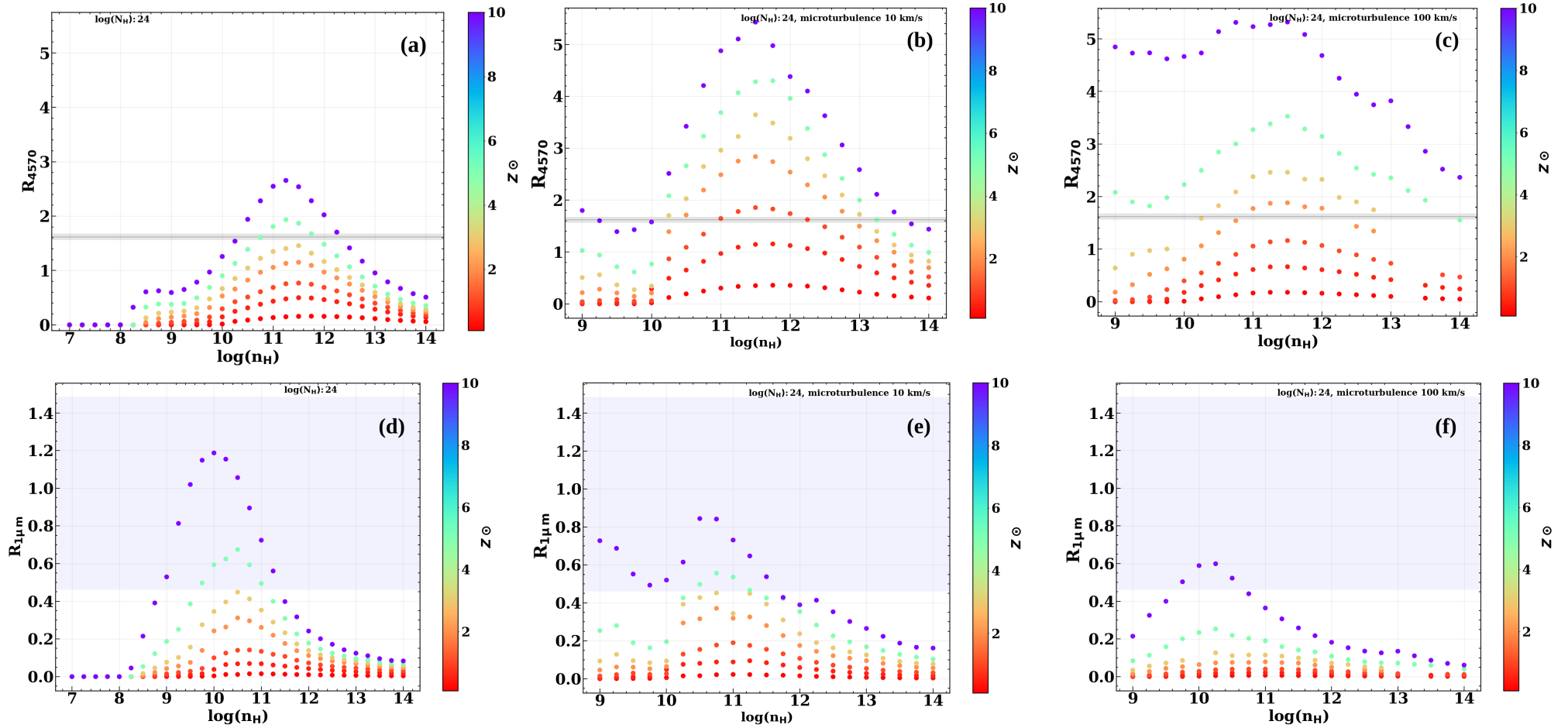


**Figure 2.** Diagnostic diagrams from simulations for  $R_{4570}$  (a–c) and  $R_{1\mu m}$  (d–f) intensities versus  $\log n_H$  for the column density  $N_H = 10^{24} \text{ cm}^{-2}$  with the microturbulent velocities,  $V_{\text{turb}} = 0 \text{ km s}^{-1}$  (a,d),  $10 \text{ km s}^{-1}$  (b,e), and  $100 \text{ km s}^{-1}$  (c,f). The color bars represent metallicities ranging from  $0.1 Z_\odot$  to  $10 Z_\odot$ . The dark gray line represents the observed value of  $R_{4570}$ , and the light gray bar shows the associated error margin. The titan white shaded region denotes the estimated values for  $R_{1\mu m}$  derived from the minimum and maximum  $\text{Pa}\beta/\text{Pa}\gamma$  ratios obtained using CLOUDY simulations. See text for details.



Although, for metallicities above solar,  $R_{1\mu\text{m}}$  values overall decrease when compared to scenarios without micro-turbulence. The  $R_{1\mu\text{m}}$  appears to be suppressed and fails to increase as expected from the optical results. For example, when the highest metallicity value of  $10 Z_{\odot}$  are considered (see Figure 2),  $V_{\text{turb}} = 10 \text{ km s}^{-1}$ , and  $100 \text{ km s}^{-1}$ , the maximum FeII ratio in the NIR is, respectively, about 0.8 and 0.6, whereas in the no-micro-turbulence case, this ratio approaches approximately 1.2 value.

To comprehend this intriguing behavior from the CLOUDY simulations observed here, Figure 3 provides a comparison of the FeII pseudo-continuum in the spectral region  $9500\text{--}11,500 \text{ \AA}$  for a fixed local hydrogen density ( $10^{10.5} \text{ cm}^{-3}$ ) for three scenarios: without micro-turbulence, with  $V_{\text{turb}} = 10$  and  $100 \text{ km s}^{-1}$ . We note that the pseudo-continuum of  $V_{\text{turb}} = 10 \text{ km s}^{-1}$  exhibits less intense lines relative to the case without micro-turbulence. The case with  $100 \text{ km s}^{-1}$  shows even weaker FeII lines. Although, for the cases with  $V_{\text{turb}} = 10$  and  $100 \text{ km s}^{-1}$ , one observes a boosting of lines, specifically between  $9600 \text{ \AA}$  and  $9900 \text{ \AA}$ , which were not distinguished in the spectrum of the no-micro-turbulence case.

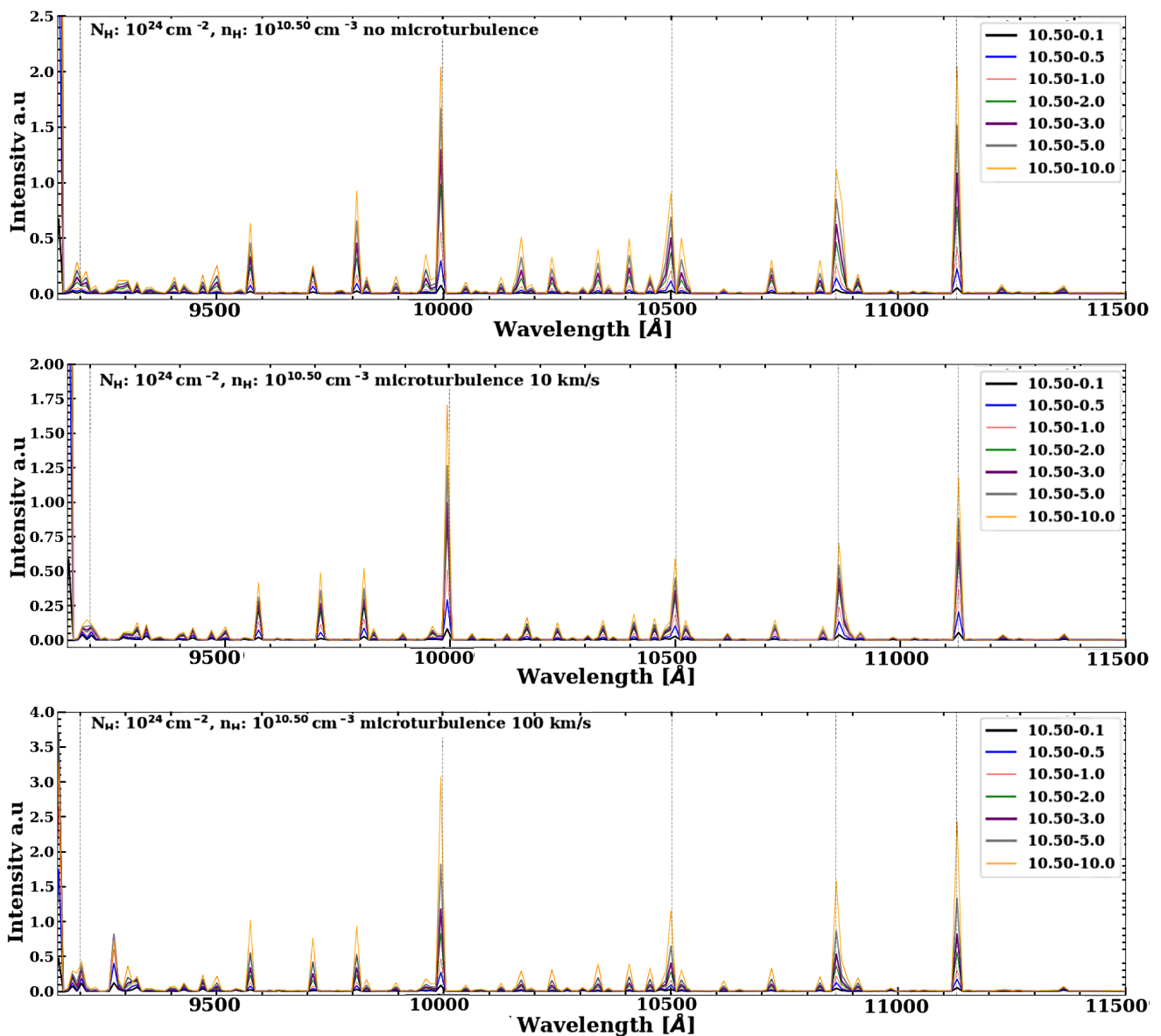
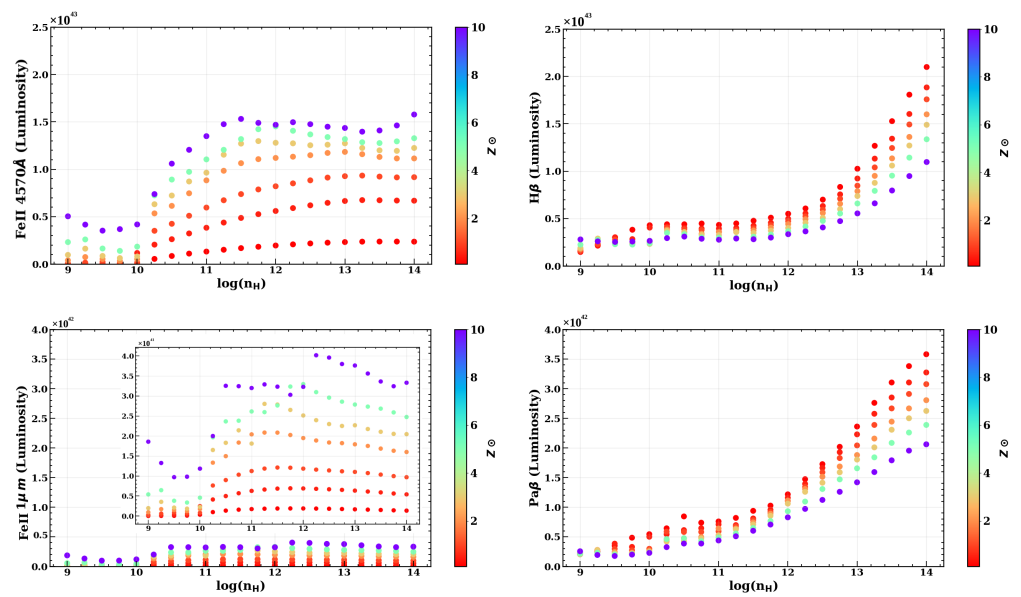


Figure 3. Predicted pseudo-continuum from CLOUDY simulations for FeII emission for the representative case of  $\log n_{\text{H}} = 10.5$  and 0.1, 0.5, 1, 2, 3, 5 and  $10 Z_{\odot}$ , as distinguished by colors, for the column density of  $10^{24} \text{ cm}^{-2}$  and zero, 10, and  $100 \text{ km s}^{-1}$  micro-turbulence velocity (top to bottom).

It is worth emphasizing that the intensity of the NIR FeII is characterized by the ratio of four isolated emissions to the Pa $\beta$  line, whereas the ratio in the optical is composed of blended FeII multiplets (m37, m38) normalized by the H $\beta$  [64,89]. Hence, to understand the variations in the  $R_{1\mu\text{m}}$ , one needs to also study the behavior of the Pa $\beta$  line across the parameter space, especially under the influence of micro-turbulence. We notice that the luminosity of the Pa $\beta$  emission significantly exceeds that of the NIR FeII lines. In contrast, in the optical range, both the H $\beta$  and the optical FeII lines exhibit a similar increase in luminosity with the density, as shown in Figures 4 and 5.

Furthermore, the 1-micron lines exhibit two significant excitation mechanisms, collisional and Lyman- $\alpha$  fluorescence, whereas the FeII bump at 9200 Å is exclusively influenced by the Lyman- $\alpha$  fluorescence mechanism [66,68]. This distinction is an important indicator of the Lyman- $\alpha$  fluorescence mechanism.

To note is that the 9200 Å region, as studied here, remains unaffected by the enhancement of micro-turbulence in the models.



**Figure 4.** Micro-turbulence case of  $10 \text{ km s}^{-1}$ . The luminosity of the 4570 Å bump (top left), the luminosity of H $\beta$  line (top right), the sum of the luminosity of the 4 FeII 1-micron lines (bottom left), and Pa $\beta$  luminosity (bottom right) versus local hydrogen density. The colors correspond to the metal content,  $Z_{\odot}$ , as indicated.

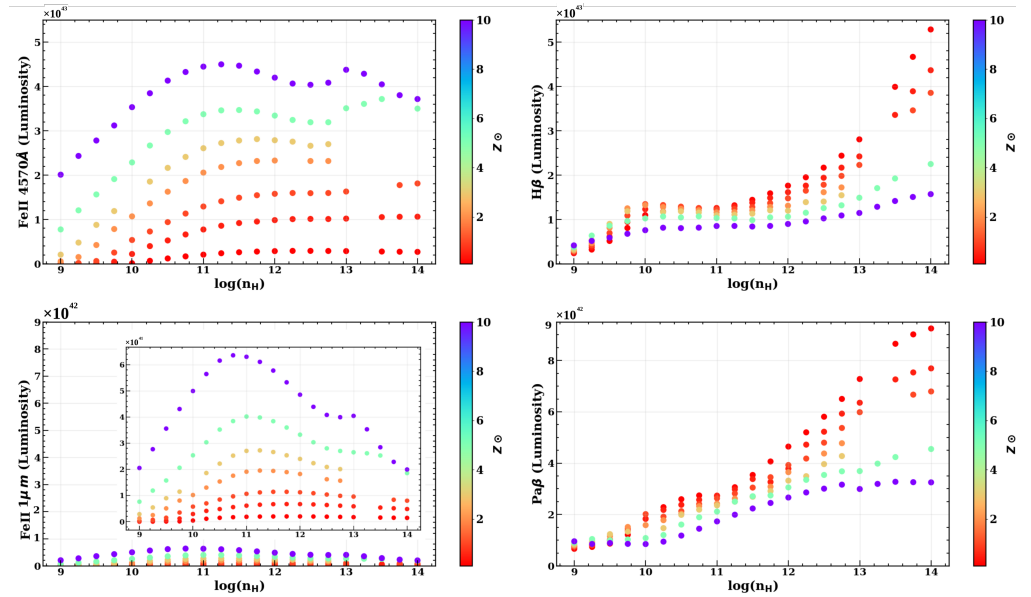


Figure 5. Same as Figure 4, but for the micro-turbulence case of  $100 \text{ km s}^{-1}$ .

## 6. Discussion

The specific influence of micro-turbulence on the NIR emission of FeII is particularly intriguing in comparison to its well-documented impact in the optical region. The optical models suggest that when micro-turbulence is introduced in the gas, this micro-turbulence enhances the intensity of the FeII lines. Surprisingly, our simulations indicated a contrasting trend in the NIR region, where the  $R_{1\mu\text{m}}$  displays lower values when micro-turbulence is considered than when micro-turbulence is absent.

The discrepancy between the measurements and CLOUDY predictions may pose a question about the true impact of micro-turbulence in the NIR. Initially, one would anticipate that the increased micro-turbulence would result in enhanced photon absorption by FeII ions, leading to an increase in the emission in this spectral region as well, as re-affirmed by the results from the FeII modeling in the optical region. This then leads to a question of whether micro-turbulence potentially influences the Lyman- $\alpha$  absorption by the FeII ion, thereby affecting NIR FeII emission [65–68]. A comprehensive investigation would be required to answer that question, but that is beyond the scope of the current investigation.

We attribute the unexpected effects observed in the 1-micron lines to a physical limitation, where we assume a fixed value for the column density as a stopping criterion for the simulations. If one allows this parameter to be set as a free parameter, this can lead to a complex interplay between the column density and the metal content in the ionized gas, as found in Ref. [73] for the case of the optical FeII emission. If this parameter is about or exceeds the value of  $10^{24.5} \text{ cm}^{-2}$ , one would obtain a cloud where the optical depth is about or higher than 1, the area where the scattering effect becomes significant; see [73] for more details. The limit at  $10^{24} \text{ cm}^{-2}$  serves to constrain the cloud's physical condition, drawing inspiration from prior investigations [73,74,90] wherein the radiative calculations are made under the optically thin regime. Thus, the non-monotonic behavior in the NIR may be ascribed to the collective influence of the micro-turbulence and cloud column density. In light of these intricate findings, further dedicated investigations are warranted to unravel the exact mechanisms at play, which also includes the advances in the available FeII atomic datasets.

Coming back to the issue of the FeII flux ratio in the NIR obtained from the observed spectrum and under the physical conditions proposed in this study, the model used is not able to replicate the ratio from Ref. [68], which is  $R_{1\mu\text{m}} \sim 1.81$ . To reproduce that value, a metal content would require to exceed  $10 Z_{\odot}$ . That would mean that the optical and NIR FeII emissions require quite different metal compositions, even though those are formed in

close vicinity to each other. This latter aspect is confirmed by the correlation observed for the FWHMs for FeII in the optical and NIR [68]. Nevertheless, exploring scenarios with significantly elevated metal content may be a possibility in future research on the NIR FeII emission, especially for high-accreting sources.

Furthermore, it is worth emphasizing the importance of investigating how the hydrogen line ratios within the BLR of an AGN vary under different physical conditions. This inquiry will significantly improve the precision of measuring the FeII ratio in the NIR for quasars with a non-reliable Pa $\beta$  line (see [39,68] for other examples). A future study to be considered, as soon as it has the potential to further refine the understanding of AGN environments and improve the accuracy of critical astrophysical measurements.

## 7. Conclusions

This study was devoted to the understanding of the line formation and physical conditions in a strong FeII emitter AGN, I Zw 1. We investigated how changes in micro-turbulence and metal content impact both the optical and NIR emissions of FeII. By introducing micro-turbulent velocities within the line-emitting cloud of 10 and 100 km s<sup>-1</sup>, employing a range 10<sup>9</sup>–10<sup>14</sup> cm<sup>-3</sup> of the cloud densities and metal content from sub-solar to 10 times solar inspired by previous studies [13,72], we explored the combined effect on the recovery of the FeII intensities. Notably, this research is the first to examine the impact of micro-turbulence in the NIR regime, especially for the FeII emission, using photoionization model predictions and corroborating them with observed flux ratios obtained from archival spectra in optical and NIR for this source. While the findings here align with prior findings made in the optical regime, we observed contrasting behavior in the NIR when micro-turbulence was introduced. Nonetheless, there is an overall agreement within the parameter ranges studied in the two wavelength regimes. A set of physical conditions can simultaneously reproduce optical and NIR FeII intensities, with  $n_{\text{H}} = 10^{10.75} - 10^{11.50} \text{ cm}^{-3}$ , and a metal content within the range  $5 Z_{\odot} \lesssim Z \lesssim 10 Z_{\odot}$ .

We reproduced the  $R_{1\mu\text{m}}$  value for I Zw 1 simultaneously in the optical region and NIR. This result is significant not only for this source but is also applicable for I Zw 1-like AGNs. The ability to replicate  $R_{1\mu\text{m}}$  values across these wavelengths is a novel accomplishment. In conclusion, a comprehensive future analysis of excitation mechanisms and FeII models holds significant promise for further insights into this complex study.

**Author Contributions:** Conceptualization, D.D.d.S. and S.P.; methodology, D.D.d.S. and S.P.; software, D.D.d.S. and M.M.; validation, D.D.d.S.; formal analysis, D.D.d.S.; investigation, D.D.d.S. and S.P.; resources, A.R.-A.; data curation, D.D.d.S., S.P., A.R.-A. and M.M.; writing—original draft preparation, D.D.d.S. and S.P.; writing—review and editing, D.D.d.S., S.P., A.R.-A. and M.M.; visualization, D.D.d.S.; supervision, A.R.-A. and S.P.; project administration, A.R.-A. and S.P.; funding acquisition, D.D.d.S. and A.R.-A. All authors have read and agreed to the published version of the manuscript.

**Funding:** This research received no external funding.

**Data Availability Statement:** Data used in this work can be provided upon request to the corresponding authors.

**Acknowledgments:** The authors thank the Brazilian Agencies: the Agency of Coordenação de Aperfeiçoamento de Pessoal de Nível Superior (CAPES), and Conselho Nacional de Desenvolvimento Científico e Tecnológico (CNPq). This study was financed in part by the Coordenação de Aperfeiçoamento de Pessoal de Nível Superior - Brasil (CAPES) - Finance Code 001. Marios Chatzikos and the CLOUDY team for giving us access to the developmental version.

**Conflicts of Interest:** The authors declare no conflicts of interest.

## Abbreviations

The following abbreviations are used in this manuscript:

AGNs	active galactic nuclei
BELR	broad-emission line region
BLR	broad-line region
CASLEO	Complejo Astronómico el Leoncito
CaT	CaII triplet
EV1	eigenvector 1
FWHM	full width at half maximum
FOS	Faint Object Spectrograph
HST	Hubble Space Telescope
IRTF	Infrared Telescope Facility
NASA	National Aeronautics and Space Administration
NIR	near-infrared
NLR	narrow-line region
NLS1	narrow-line Seyfert 1
PCA	principal component analysis
SMBHs	supermassive black holes
SXD	short wavelength cross-dispersed mode
UV	ultraviolet
Zw	Zwicky

## Appendix A

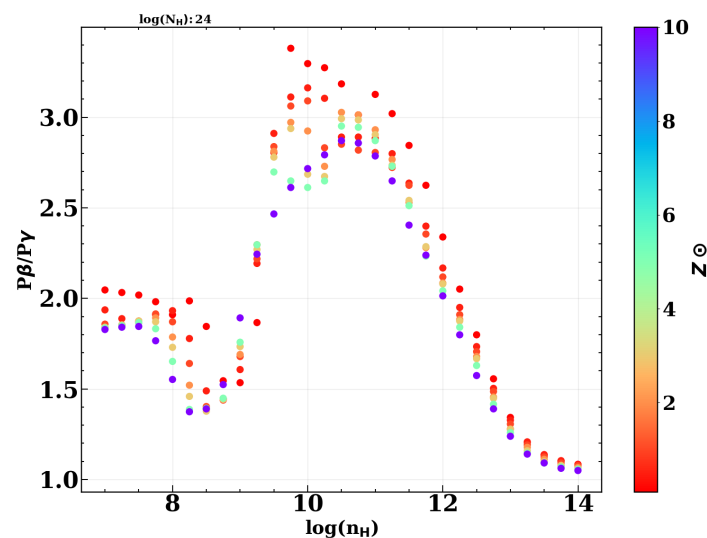


**Figure A1.** The luminosity ratio for Pa $\beta$  to Pa $\gamma$  obtained from simulations used here for a range of local hydrogen densities,  $n_{\text{H}}$ . The colors correspond to the different metal content. The cloud column density is  $10^{24} \text{ cm}^{-2}$  at zero micro-turbulence.

## References

1. Netzer, H. Revisiting the unified model of active galactic nuclei. *Annu. Rev. Astron. Astrophys.* **2015**, *53*, 365–408. [[CrossRef](#)]
2. Padovani, P.; Alexander, D.M.; Assef, R.J.; De Marco, B.; Giommi, P.; Hickox, R.C.; Richards, G.T.; Smolčić, V.; Hatziminaoglou, E.; Mainieri, V.; et al. Active galactic nuclei: What's in a name? *Astron. Astrophys. Rev.* **2017**, *25*, 2. [[CrossRef](#)]
3. Collin, S.; Kawaguchi, T.; Peterson, B.M.; Vestergaard, M. Systematic effects in measurement of black hole masses by emission-line reverberation of active galactic nuclei: Eddington ratio and inclination. *Astron. Astrophys.* **2006**, *456*, 75–90. [[CrossRef](#)]
4. Panda, S.; Marziani, P.; Czerny, B. The quasar main sequence explained by the combination of Eddington ratio, metallicity, and orientation. *Astrophys. J.* **2019**, *882*, 79. [[CrossRef](#)]
5. Antonucci, R. Unified models for active galactic nuclei and quasars. *Annu. Rev. Astron. Astrophys.* **1993**, *31*, 473–521. [[CrossRef](#)]
6. Urry, C. M.; Padovani, P. Unified schemes for radio-loud active galactic nuclei. *Publ. Astron. Soc. Pac.* **1995**, *107*, 803–845. [[CrossRef](#)]



7. Sulentic, J.W.; Marziani, P.; Dultzin-Hacyan, D. Phenomenology of broad emission lines in active galactic nuclei. *Annu. Rev. Astron. Astrophys.* **2000**, *38*, 521–571. [[CrossRef](#)]
8. Blandford, R.D.; McKee, C.F. Reverberation mapping of the emission line regions of Seyfert galaxies and quasars. *Astrophys. J.* **1982**, *255*, 419–439. [[CrossRef](#)]
9. Peterson, B.M.; Ferrarese, L.; Gilbert, K.M.; Kaspi, S.; Malkan, M.A.; Maoz, D.; Merritt, D.; Netzer, H.; Onken, C.A.; Pogge, R.W.; et al. Central masses and broad-line region sizes of active galactic nuclei. II. A homogeneous analysis of a large reverberation-mapping database. *Astrophys. J.* **2004**, *613*, 682–699. [[CrossRef](#)]
10. Bentz, M.C.; Denney, K.D.; Grier, C.J.; Barth, A.J.; Peterson, B.M.; Vestergaard, M.; Bennert, V.N.; Canalizo, G.; De Rosa, G.; Filippenko, A.V.; et al. The low-luminosity end of the radius–luminosity relationship for active galactic nuclei. *Astrophys. J.* **2013**, *767*, 149. [[CrossRef](#)]
11. Du, P. et al. [SEAMBH Collaboration]. Supermassive black holes with high accretion rates in active galactic nuclei. IV. H $\beta$  time lags and implications for super-Eddington accretion. *Astrophys. J.* **2015**, *806*, 22. [[CrossRef](#)]
12. Grier, C.J.; Pancoast, A.; Barth, A.J.; Fausnaugh, M.M.; Brewer, B.J.; Treu, T.; Peterson, B.M. The structure of the broad-line region in active galactic nuclei. II. Dynamical modeling of data from the AGN10 reverberation mapping campaign. *Astrophys. J.* **2017**, *849*, 146. [[CrossRef](#)]
13. Panda, S.; Martínez-Aldama, M.L.; Zajaček, M. Current and future applications of Reverberation-mapped quasars in cosmology. *Front. Astron. Space Sci.* **2019**, *6*, 75. [[CrossRef](#)]
14. Shen, Y.; Grier, C.J.; Horne, K.; Stone, Z.; Li, J.I.; Yang, Q.; Homayouni, Y.; Trump, J.R.; Anderson, S.F.; Brandt, W.N.; et al. The Sloan Digital Sky Survey Reverberation Mapping project: Key results. *arXiv* **2023**, arXiv:2305.01014.
15. Peterson, B.M.; Ali, B.; Horne, K.; Bertram, R.; Lame, N.J.; Pogge, R.W.; Wagner, R.M. The structure of the broad-line region in the Seyfert galaxy Markarian 590. *Astrophys. J.* **1993**, *402*, 469–478. [[CrossRef](#)]
16. Peterson, B.M.; Berlind, P.; Bertram, R.; Bochkarev, N.G.; Bond, D.; Brotherton, M.S.; Busler, J.R.; Chuvpov, K.K.; Cohen, R.D.; Dietrich, M.; et al. Steps toward determination of the size and structure of the broad-line region in active galactic nuclei. VII. Variability of the optical spectrum of NGC 5548 over 4 years. *Astrophys. J.* **1994**, *425*, 622–634. [[CrossRef](#)]
17. Rosenblatt, E.I.; Malkan, M.A.; Sargent, W.L.W.; Readhead, A.C.S. The broad emission line and continuum variations of Seyfert galaxies. II. Broad-line region structure and kinematics. *Astrophys. J. Suppl.* **1994**, *93*, 73–124. [[CrossRef](#)]
18. Korista, K.T.; Alloin, D.; Barr, P.; Clavel, J.; Cohen, R.D.; Crenshaw, D.M.; Evans, I.N.; Horne, K.; Koratkar, A.P.; Kriss, G.A.; et al. Steps toward determination of the size and structure of the broad-line region in active galactic nuclei. VIII. An intensive *HST*, *IUE*, and ground-based study of NGC 5548. *Astrophys. J. Suppl.* **1995**, *97*, 285–330. [[CrossRef](#)]
19. Veilleux, S.; Sanders, D.B.; Kim, D.-C. A near-infrared search for hidden broad-line regions in ultraluminous infrared galaxies. *Astrophys. J.* **1997**, *484*, 92–107. [[CrossRef](#)]
20. Vanden Berk, D.E.; Richards, G.T.; Bauer, A.; Strauss, M.A.; Schneider, D.P.; Heckman, T.M.; York, D.G.; Hall, P.B.; Fan, X.; Knapp, G.R.; et al. Composite quasar spectra from the Sloan Digital Sky Survey. *Astron. J.* **2001**, *122*, 549–564. [[CrossRef](#)]
21. Kollatschny, W. Accretion disk wind in the AGN broad-line region: Spectroscopically resolved line profile variations in Mrk 110. *Astron. Astrophys.* **2003**, *407*, 461–472. [[CrossRef](#)]
22. Glikman, E.; Helfand, D.J.; White, R.L. A near-infrared spectral template for quasars. *Astrophys. J.* **2006**, *640*, 579–591. [[CrossRef](#)]
23. Vestergaard, M.; Peterson, B.M. Determining central black hole masses in distant active galaxies and quasars. II. Improved optical and UV scaling relationships. *Astrophys. J.* **2006**, *641*, 689–709. [[CrossRef](#)]
24. Marziani, P.; Sulentic, J.W.; Negrete, C.A.; Dultzin, D.; Zamfir, S.; Bachev, R. Broad-line region physical conditions along the quasar eigenvector 1 sequence. *Mon. Not. R. Astron. Soc.* **2010**, *409*, 1033–1048. [[CrossRef](#)]
25. Pozo Nuñez, F.; Ramolla, M.; Westhues, C.; Haas, M.; Chini, R.; Steenbrugge, K.; Barr Domínguez, A.; Kaderhandt, L.; Hackstein, M.; Kollatschny, W.; et al. The broad-line region and dust torus size of the Seyfert 1 galaxy PGC 50427. *Astron. Astrophys.* **2015**, *576*, A73. [[CrossRef](#)]
26. Marziani, P.; Dultzin, D.; Sulentic, J.W.; Del Olmo, A.; Negrete, C.A.; Martínez-Aldama, M.L.; D’Onofrio, M.; Bon, E.; Bon, N.; Stirpe, G.M. A main sequence for quasars. *Front. Astron. Space Sci.* **2018**, *5*, 6. [[CrossRef](#)]
27. MacLeod, C.L.; Green, P.J.; Anderson, S.F.; Bruce, A.; Eracleous, M.; Graham, M.; Homan, D.; Lawrence, A.; LeBleu, A.; Ross, N.P.; et al. Changing-look quasar candidates: First results from follow-up spectroscopy of highly optically variable quasars. *Astrophys. J.* **2019**, *874*, 8. [[CrossRef](#)]
28. Wolf, J.; Salvato, M.; Coffey, D.; Merloni, A.; Buchner, J.; Arcodia, R.; Baron, D.; Carrera, F.J.; Comparat, J.; Schneider, D.P.; et al. Exploring the diversity of Type 1 active galactic nuclei identified in SDSS-IV/SPIDERS. *Mon. Not. R. Astron. Soc.* **2020**, *492*, 3580–3601. [[CrossRef](#)]
29. Fonseca Alvarez, G.; Trump, J.R.; Homayouni, Y.; Grier, C.J.; Shen, Y.; Horne, K.; Li, J.I.-H.; Brandt, W.N.; Ho, L.C.; Peterson, B.M.; et al. The Sloan Digital Sky Survey Reverberation Mapping project: The H $\beta$  radius–luminosity relation. *Astrophys. J.* **2020**, *899*, 73. [[CrossRef](#)]
30. Rakshit, S. Broad line region and black hole mass of PKS 1510-089 from spectroscopic reverberation mapping. *Astron. Astrophys.* **2020**, *642*, A59. [[CrossRef](#)]

31. Schindler, J.-T.; Farina, E.P.; Bañados, E.; Eilers, A.-C.; Hennawi, J.F.; Onoue, M.; Venemans, B.P.; Walter, F.; Wang, F.; Davies, F.B.; et al. The X-SHOOTER/ALMA sample of quasars in the epoch of reionization. I. NIR spectral modeling, iron enrichment, and broad emission line properties. *Astrophys. J.* **2020**, *905*, 51. [CrossRef]
32. Li, S.-S.; Feng, H.-C.; Liu, H.T.; Bai, J.M.; Li, R.; Lu, K.-X.; Wang, J.-G.; Huang, Y.-K.; Zhang, Z.-X. Velocity-resolved reverberation mapping of changing-look active galactic nucleus NGC 4151 during outburst stage: Evidence for kinematics evolution of broad-line region. *Astrophys. J.* **2022**, *936*, 75. [CrossRef]
33. Pandey, S.; Rakshit, S.; Woo, J.-H.; Stalin, C.S. Spectroscopic reverberation mapping of quasar PKS 0736 + 017: Broad-line region and black-hole mass. *Mon. Not. R. Astron. Soc.* **2022**, *516*, 2671–2682. [CrossRef]
34. Lu, K.-X.; Bai, J.-M.; Wang, J.M.; Hu, C.; Li, Y.-R.; Du, P.; Xiao, M.; Feng, H.C.; Li, S.-S.; Wang, J.-G.; et al. Supermassive black hole and broad-line region in NGC 5548: Results from five-season reverberation mapping. *Astrophys. J. Suppl. Ser.* **2022**, *263*, 10. [CrossRef]
35. Bentz, M.C.; Onken, C.A.; Street, R.; Valluri, M. Reverberation mapping of IC 4329A. *Astrophys. J.* **2023**, *944*, 29. [CrossRef]
36. Donnan, F.R.; Hernández Santisteban, J.V.; Horne, K.; Hu, C.; Du, P.; Li, Y.-R.; Xiao, M.; Ho, L.C.; Aceituno, J.; Wang, J.-M.; et al. Testing super-eddington accretion on to a supermassive black hole: Reverberation mapping of PG 1119+120. *Mon. Not. R. Astron. Soc.* **2023**, *523*, 545–567. [CrossRef]
37. Wills, B.J.; Netzer, H.; Wills, D. Broad emission features in QSOs and active galactic nuclei. II. New observations and theory of Fe II and H I emission. *Astrophys. J.* **1985**, *288*, 94–116. [CrossRef]
38. Verner, E.M.; Verner, D.A.; Korista, K.T.; Ferguson, J.W.; Hamann, F.; Ferland, G.J. Numerical simulations of Fe II emission spectra. *Astrophys. J. Suppl. Ser.* **1999**, *120*, 101–112. [CrossRef]
39. Marinello, M.; Rodríguez-Ardila, A.; Marziani, P.; Sigut, A.; Pradhan, A. Panchromatic properties of the extreme Fe II emitter PHL 1092. *Mon. Not. R. Astron. Soc.* **2020**, *494*, 4187–4202. [CrossRef]
40. Phillips, M.M. Observations of Fe II emission in Seyfert galaxies and QSOs. *Astrophys. J.* **1977**, *215*, 746–754. [CrossRef]
41. Sigut, T.A.A.; Pradhan, A.K. Predicted Fe II emission-line strengths from active galactic nuclei. *Astrophys. J. Suppl. Ser.* **2003**, *145*, 15–37. [CrossRef]
42. Sigut, T.A.A.; Pradhan, A.K.; Nahar, S.N. Theoretical Fe I–III emission-line strengths from active galactic nuclei with broad-line regions. *Astrophys. J.* **2004**, *611*, 81–92. [CrossRef]
43. Hamann, F.; Ferland, G. The age and chemical evolution of high-redshift QSOs. *Astrophys. J.* **1992**, *391*, L53–L57. [CrossRef]
44. Baldwin, J.A.; Ferland, G.J.; Korista, K.T.; Hamann, F.; LaCluzé, A. The origin of Fe II emission in active galactic nuclei. *Astrophys. J.* **2004**, *615*, 610–624. [CrossRef]
45. Martínez-Aldama, M.L.; Panda, S.; Czerny, B.; Marinello, M.; Marziani, P.; Dultzin, D. The CaFe project: Optical Fe II and near-infrared Ca II triplet emission in active galaxies. II. The driver(s) of the Ca II and Fe II and its potential use as a chemical clock. *Astrophys. J.* **2021**, *918*, 29. [CrossRef]
46. Sarkar, A.; Ferland, G.J.; Chatzikos, M.; Guzmán, F.; van Hoof, P.A.M.; Smyth, R.T.; Ramsbottom, C.A.; Keenan, F.P.; Ballance, C.P. Improved Fe II emission-line models for AGNs using new atomic data sets. *Astrophys. J.* **2021**, *907*, 12. [CrossRef]
47. Boroson, T.A.; Green, R.F. The emission-line properties of low-redshift quasi-stellar objects. *Astrophys. J. Suppl. Ser.* **1992**, *80*, 109–135. [CrossRef]
48. Phillips, M.M. The optical spectrum of I Zwicky 1. *Astrophys. J.* **1976**, *208*, 37–41. [CrossRef]
49. Oke, J.B.; Lauer, T.R. An analysis of the spectra of the Seyfert galaxies Markarian 79 and I Zw 1. *Astrophys. J.* **1979**, *230*, 360–372. [CrossRef]
50. Joly, M. The FeII spectrum of Seyfert 1 galaxies and quasars. *Astron. Astrophys.* **1981**, *102*, 321–330. Available online: <https://ui.adsabs.harvard.edu/abs/1981A%26A...102..321J%2F/> (accessed on 3 January 2024).
51. Halpern, J.P.; Oke, J.B. Narrow-line Seyfert galaxies with permitted Fe II emission: Markarian 507, 5C 3.100, and I Zwicky 1. *Astrophys. J.* **1987**, *312*, 91–100. [CrossRef]
52. Laor, A.; Jannuzi, B.T.; Green, R.F.; Boroson, T.A. The ultraviolet properties of the narrow-line quasar I Zw 1. *Astrophys. J.* **1997**, *489*, 656–671. [CrossRef]
53. Negrete, C.A.; Dultzin, D.; Marziani, P.; Sulentic, J.W. Broad-line region physical conditions in extreme population A quasars: A method to estimate central black hole mass at high redshift. *Astrophys. J.* **2012**, *757*, 62. [CrossRef]
54. Park, D.; Barth, A.J.; Ho, L.C.; Laor, A. A new iron emission template for active galactic nuclei. I. Optical template for the H $\beta$  region. *Astrophys. J. Suppl.* **2022**, *258*, 38. [CrossRef]
55. Sulentic, J.W.; Zwitter, T.; Marziani, P.; Dultzin-Hacyan, D. Eigenvector 1: An optimal correlation space for active galactic nuclei. *Astrophys. J. Lett.* **2000**, *536*, L5–L9. [CrossRef]
56. Shen, Y.; Ho, L.C. The diversity of quasars unified by accretion and orientation. *Nature* **2014**, *513*, 210–213. [CrossRef]
57. Deconto-Machado, A.; del Olmo Orozco, A.; Marziani, P.; Perea, J.; Stirpe, G.M. High-redshift quasars along the main sequence. *Astron. Astrophys.* **2023**, *669*, A83. [CrossRef]
58. Mengistue, S.T.; Del Olmo, A.; Marziani, P.; Pović, M.; Martínez-Carballo, M.A.; Perea, J.; Márquez, I. Optical and near-UV spectroscopic properties of low-redshift jetted quasars in the main sequence context. *Mon. Not. R. Astron. Soc.* **2023**, *525*, 4474–4496. [CrossRef]
59. Vestergaard, M.; Wilkes, B.J. An empirical ultraviolet template for iron emission in quasars as derived from I Zwicky 1. *Astrophys. J. Suppl. Ser.* **2001**, *134*, 1–33. [CrossRef]

60. Tsuzuki, Y.; Kawara, K.; Yoshii, Y.; Oyabu, S.; Tanabé, T.; Matsuoka, Y. Fe II emission in 14 low-redshift quasars. I. Observations. *Astrophys. J.* **2006**, *650*, 57–79. [[CrossRef](#)]
61. Kovačević-Dojčinović, J.; Popović, L.Č. The connections between the UV and optical Fe II emission lines in type 1 AGNs. *Astrophys. J. Suppl. Ser.* **2015**, *221*, 35. [[CrossRef](#)]
62. Dong, X.-B.; Ho, L.C.; Wang, J.-G.; Wang, T.-G.; Wang, H.; Fan, X.; Zhou, H. The prevalence of narrow optical Fe II emission lines in type 1 active galactic nuclei. *Astrophys. J. Lett.* **2010**, *721*, L143–L147. [[CrossRef](#)]
63. Dong, X.-B.; Wang, J.-G.; Ho, L.C.; Wang, T.-G.; Fan, X.; Wang, H.; Zhou, H.; Yuan, W. What controls the Fe II strength in active galactic nuclei? *Astrophys. J.* **2011**, *736*, 86. [[CrossRef](#)]
64. Kovačević, J.; Popović, L.Č.; Dimitrijević, M.S. Analysis of optical Fe II emission in a sample of active galactic nucleus spectra. *Astrophys. J. Suppl. Ser.* **2010**, *189*, 15–36. [[CrossRef](#)]
65. Sigut, T.A.A.; Pradhan, A.K. Ly $\alpha$  fluorescent excitation of Fe II in active galactic nuclei. *Astrophys. J.* **1998**, *499*, L139–L142. [[CrossRef](#)]
66. Rodríguez-Ardila, A.; Viegas, S.M.; Pastoriza, M.G.; Prato, L. Infrared Fe II emission in narrow-line Seyfert 1 galaxies. *Astrophys. J.* **2002**, *565*, 140. [[CrossRef](#)]
67. Garcia-Rissmann, A.; Rodríguez-Ardila, A.; Sigut, T.A.A.; Pradhan, A.K. A near-infrared template derived from I Zw 1 for the Fe II emission in active galaxies. *Astrophys. J.* **2012**, *751*, 7. [[CrossRef](#)]
68. Marinello, M.; Rodríguez-Ardila, A.; Garcia-Rissmann, A.; Sigut, T.A.A.; Pradhan, A.K. The Fe II emission in active galactic nuclei: Excitation mechanisms and location of the emitting region. *Astrophys. J.* **2016**, *820*, 116. [[CrossRef](#)]
69. Rudy, R.J.; Mazuk, S.; Puetter, R.C.; Hamann, F. The 1 micron Fe II lines of the seyfert galaxy I Zw 1. *Astrophys. J.* **2000**, *539*, 166–171. [[CrossRef](#)]
70. Riffel, R.; Rodríguez-Ardila, A.; Pastoriza, M.G. A 0.8–2.4  $\mu\text{m}$  spectral atlas of active galactic nuclei. *Astron. Astrophys.* **2006**, *457*, 61–70. [[CrossRef](#)]
71. Martínez-Aldama, M.L.; Dultzin, D.; Marziani, P.; Sulentic, J.W.; Bressan, A.; Chen, Y.; Stirpe, G.M. OI and Ca II observations in intermediate redshift quasars. *Astrophys. J. Suppl. Ser.* **2015**, *217*, 3. [[CrossRef](#)]
72. Panda, S.; Martínez-Aldama, M.L.; Marinello, M.; Czerny, B.; Marziani, P.; Dultzin, D. The CaFe project: Optical Fe II and near-infrared Ca II triplet emission in active galaxies. I. Photoionization modeling. *Astrophys. J.* **2020**, *902*, 76. [[CrossRef](#)]
73. Panda, S. The CaFe project: Optical Fe II and near-infrared Ca II triplet emission in active galaxies: Simulated EWs and the co-dependence of cloud size and metal content. *Astron. Astrophys.* **2021**, *650*, A154. [[CrossRef](#)]
74. Bruhweiler, F.; Verner, E. Modeling Fe II emission and revised Fe II (UV) empirical templates for the Seyfert 1 galaxy I Zw 1. *Astrophys. J.* **2008**, *675*, 83–95. [[CrossRef](#)]
75. Panda, S.; Czerny, B.; Adhikari, T.P.; Hryniewicz, K.; Wildy, C.; Kuraszkiewicz, J.; Śniegowska, M. Modeling of the quasar main sequence in the optical plane. *Astrophys. J.* **2018**, *866*, 115. [[CrossRef](#)]
76. Dias dos Santos, D.; Panda, S.; Rodríguez-Ardila, A.; Marinello, M. Modelling the strong Fe II emission. *Bol. Soc. Astron. Bras.* **2023**, *34*, 295–299. Available online: <https://sab-astro.org.br/sab/publicacoes/boletim-da-sab-vol-34/> (accessed on 3 January 2024).
77. Panda, S.; Czerny, B.; Done, C.; Kubota, A. CLOUDY view of the warm corona. *Astrophys. J.* **2019**, *875*, 133. [[CrossRef](#)]
78. Ferland, G.J.; Chatzikos, M.; Guzmán, F.; Lykins, M.L.; van Hoof, P.A.M.; Williams, R.J.R.; Abel, N.P.; Badnell, N.R.; Keenan, F.P.; Porter, R.L.; et al. The 2017 release of CLOUDY. *Rev. Mex. Astron. Astrofis.* **2017**, *53*, 385–438. Available online: <http://www.astroscu.unam.mx/rmaa/RMxAA..53-2/> (accessed on 3 January 2024).
79. Véron-Cetty, M.-P.; Joly, M.; Véron, P. The unusual emission line spectrum of I Zw 1. *Astron. Astrophys.* **2004**, *417*, 515–525. [[CrossRef](#)]
80. Huang, Y.-K.; Hu, C.; Zhao, Y.-L.; Zhang, Z.-X.; Lu, K.-X.; Wang, K.; Zhang, Y.; Du, P.; Li, Y.-R.; Bai, J.-M.; et al. Reverberation mapping of the narrow-line Seyfert 1 galaxy I Zwicky 1: Black hole mass. *Astrophys. J.* **2019**, *876*, 102. [[CrossRef](#)]
81. Osterbrock, D.E.; Pogge, R.W. The spectra of narrow-line Seyfert 1 galaxies. *Astrophys. J.* **1985**, *297*, 166–176. [[CrossRef](#)]
82. Marziani, P.; del Olmo, A.; Negrete, C.A.; Dultzin, D.; Piconcelli, E.; Vietri, G.; Martínez-Aldama, M.L.; D’Onofrio, M.; Bon, E.; Bon, N.; et al. The intermediate-ionization lines as virial broadening estimators for Population A quasars. *Astrophys. J. Suppl. Ser.* **2022**, *261*, 30. [[CrossRef](#)]
83. Kaspi, S.; Smith, P.S.; Netzer, H.; Maoz, D.; Jannuzi, B.T.; Giveon, U. Reverberation measurements for 17 quasars and the size-mass-luminosity relations in active galactic nuclei. *Astrophys. J.* **2000**, *533*, 631–649. [[CrossRef](#)]
84. Panda, S. Physical conditions in the low-ionization broad-line region in active galaxies. *Publ. Astronom. Observat. Belgr.* **2021**, *100*, 333–338. Available online: <https://ui.adsabs.harvard.edu/abs/2021POBeo.100..333P/> (accessed on 3 January 2024).
85. Grevesse, N.; Asplund, M.; Sauval, A.J.; Scott, P. The chemical composition of the sun. *Can. J. Phys.* **2011**, *89*, 327–331. [[CrossRef](#)]
86. Bottorff, M.C.; Ferland, G.J. Magnetic confinement, magnetohydrodynamic waves and smooth line profiles in active galactic nuclei. *Mon. Not. R. Astron. Soc.* **2000**, *316*, 103–106. [[CrossRef](#)]
87. Rees, M.J. Magnetic confinement of broad-line clouds in active galactic nuclei. *Mon. Not. R. Astron. Soc.* **1987**, *228*, 47P–50P. [[CrossRef](#)]
88. Kollatschny, W.; Zetzl, M. The shape of broad-line profiles in active galactic nuclei. *Astron. Astrophys.* **2013**, *549*, A100. [[CrossRef](#)]

- 
89. Marziani, P.; Berton, M.; Panda, S.; Bon, E. Optical singly-ionized iron emission in radio-quiet and relativistically jetted active galactic nuclei. *Universe* **2021**, *7*, 484. [[CrossRef](#)]
  90. Ferland, G.J.; Persson, S.E. Implications of Ca II emission for physical conditions in the broad-line region of active galactic nuclei. *Astrophys. J.* **1989**, *347*, 656–673. [[CrossRef](#)]

**Disclaimer/Publisher’s Note:** The statements, opinions and data contained in all publications are solely those of the individual author(s) and contributor(s) and not of MDPI and/or the editor(s). MDPI and/or the editor(s) disclaim responsibility for any injury to people or property resulting from any ideas, methods, instructions or products referred to in the content.